Carbonized Nanoscale Metal–Organic Frameworks as High Performance Electrocatalyst for Oxygen Reduction Reaction

Shenlong Zhao,[†,‡,§] Huajie Yin,[‡] Lei Du,[∥] Liangcan He,[‡] Kun Zhao,[‡] Lin Chang,[‡] Geping Yin,[‡] Huijun Zhao,[⊥] Shaoqin Liu,[*,†,§] and Zhiyong Tang[*,‡]

[†]School of Materials Science and Engineering, and [§]Center for Micro and Nanotechnology, Harbin Institute of Technology, Harbin 150080, P. R. China, [‡]Laboratory for Nanosystem and Hierarchy Fabrication, National Center for Nanoscience and Technology, Beijing 100190, P. R. China, [∥]Institute of Advanced Chemical Power Sources, School of Chemical Engineering and Technology, Harbin Institute of Technology, Harbin 150001, P. R. China, and [⊥]Centre for Clean Environment and Energy, Griffith University, Gold Coast Campus, Gold Coast, QLD 4222, Australia

ABSTRACT The oxygen reduction reaction (ORR) is one of the key steps in clean and efficient energy conversion techniques such as in fuel cells and metal–air batteries; however, several disadvantages of current ORRs including the kinetically sluggish process and expensive catalysts hinder mass production of these devices. Herein, we develop carbonized nanoparticles, which are derived from monodisperse nanoscale metal organic frameworks (MIL-88B-NH_3), as the high performance ORR catalysts. The onset potential and the half-wave potential for the ORR at these carbonized nanoparticles is up to 1.03 and 0.92 V (*vs* RHE) in 0.1 M KOH solution, respectively, which represents the best ORR activity of all the non-noble metal catalysts reported so far. Furthermore, when used as the cathode of the alkaline direct fuel cell, the power density obtained with the carbonized nanoparticles reaches 22.7 mW/cm^2, 1.7 times higher than the commercial Pt/C catalysts.

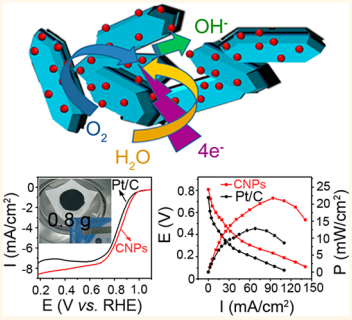

KEYWORDS: carbonization · direct methanol fuel cell · metal organic framework · oxygen reduction reaction

The catalytic oxygen reduction in basic solution is a crucial cathodic reaction for numerous promising renewable-energy technologies such as in alkaline fuel cells and metal–air batteries.[1−6] Unfortunately, the electrocatalysts currently in use for the oxygen reduction reaction (ORR) cannot meet the application requirements of high catalytic activity, good durability, and low cost,[7−13] greatly limiting the practical use of such innovative technologies. As an example, platinum (Pt)-based electrocatalysts have been the best ORR electrocatalysts in basic media, but their widespread use has been severely limited by the high cost and scarcity.[14−20] Therefore, tremendous efforts have been devoted to synthesize high performance, inexpensive, and earth-abundant materials-based ORR electrocatalysts to replace Pt.[21−29] Among different synthetic strategies, pyrolysis of the hybrids of organic molecules/polymers and transition metal ions has been demonstrated as a very effective approach for obtaining non-noble-metal electrocatalysts due to simple operation, significant cost-saving, and easy scale-up.[30−35] However, the overall performance for the majority of such electrocatalysts still cannot compete with conventional Pt-based electrocatalysts, mainly due to their rather low catalytic activity.[8,9] A widely accepted reason for the low catalytic activity is the lack of accurate control over the size, shape, and structure of the organic–inorganic hybrid precursors, giving rise to nonuniform and insufficient exposure of the active catalytic sites of the pyrolytic products.[29−31]

In this work, we propose to use nanoscale metal–organic frameworks (MOFs) with controllable size and shape as the pyrolytic precursors to achieve high performance ORR catalysts. This idea is mainly based on two considerations. First, MOFs represent a new family of crystalline framework materials (more than 6000 members) made by linking metal ions (Zn, Fe, Co, *etc.*) and

* Address correspondence to shaoqinliu@hit.edu.cn, zytang@nanoctr.cn.

Received for review October 1, 2014 and accepted November 26, 2014.

Published online November 26, 2014
10.1021/nn505582e

organic moieties (synthetic small molecule, amino acid, peptides, *etc.*) through coordination interactions.[36,37] Thanks to their diverse composition, ultrahigh surface area, and ordered and controllable porous structure, MOFs offer an opportunity to obtain high performance non-noble-metal electrocatalysts if the porosity and uniformity of the catalytic active sites can be inherited after pyrolysis.[38] Second, compared with bulk materials, nanoscale materials have a much greater capability to resist drastic structural/morphological damage caused by high temperature pyrolysis,[33,38,39] and the larger surface-to-volume ratio would also benefit electrocatalytic reactions if the sizes of the pyrolytic products could be kept in the nanometer scale.[40,41] It should be pointed out that to adopt carbonized MOFs as ORR catalysts has been recently reported by utilizing Zn-based MOFs as the self-sacrificed precursors.[42−45] Removal of easily evaporated Zn elements at a high calcination temperature gives rise to the generation of porous carbon catalysts for ORR. However, different from the well-defined pore structure of original Zn-based MOFs precursors, the pores of as-carbonized products caused by Zn evaporation generally have a wide size distribution, and furthermore removal of Zn elements eliminates possible catalytically active sites from transition metals,[29,46] thus causing that their ORR catalytic activity is still lower than the desirable value. Therefore, how to prepare the carbonized products, which could preserve unique characteristics of MOFs precursors including well-defined pore structure and size, rich chemical composition, and homogeneous distribution of the composed elements, is becoming the key to achieve the non-noble-metal catalysts with ORR activity better than conventional Pt/C catalysts.

RESULTS AND DISCUSSION

An Fe-based MOFs nanoparticle (NP), MIL-88B-NH_3 [$Fe_3O(H_2N\text{-}BDC)_3$, H_2N-BDC = 2-aminoterephtalic acid], is chosen as an ideal precursor for high-performance ORR electrocatalyst. Figure 1 illustrates our selection criteria. The Fe-based MOFs with N, O-containing organic ligands are preferred. These MOFs provide the opportunity to produce the highly active species for ORR such as Fe/Fe_3C−C after pyrolyzing at 900 °C.[30] In addition, the Fe and N codoped carbon materials have better conductivity than pure carbon, which would benefit electrochemical reactions such as ORR.[30,31,46−48] Lastly, the porosity could prompt diffusion of both reactants (O_2) and products (OH^-) if it is maintained.

The spindle-like MIL-88B-NH_3 NPs with uniform diameters of ∼50 nm and lengths of ∼140 nm (Figure 2a and Supporting Information Figure S1a) were first synthesized according to the previously reported hydrothermal method with slight modification.[49] Subsequently, as-synthesized MIL-88B-NH_3 NPs were converted into the carbonized NPs (CNPs) by heat treatment at 900 °C in Ar

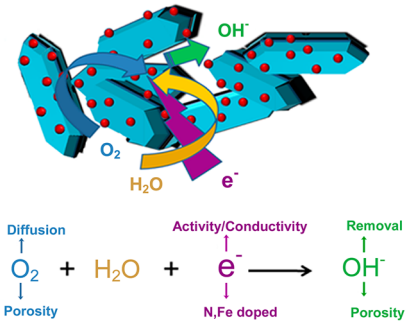

Figure 1. Principle of high performance electrocatalysts for oxygen reduction reaction in alkaline solution.

for 6 h. Notably, the transmission electron miscopy (TEM) and scanning electron microscopy (SEM) images show that both shape and size of the CNPs remained intact after the pyrolysis process (Figure 2b and Figure S1b). This result is in a sharp contrast to the carbonized products from large-sized MIL88B-NH_3 microparticles (CMPs), and the microstructures are obviously collapsed accompanied with appearance of many small particles on the CMP surfaces (Figure S2). A noticeable difference between CNPs and CMPs can be further revealed by specific surface area analysis and pore measurement. As-synthesized MIL-88B-NH_3 NPs have a rather low porosity of 203 m^2/g and broad pore distribution (Figure S3a and Table S1), likely caused by partial blockage of the added PluronicF127 surfactant that is used during synthesis to control the growth of MOF NPs. Interestingly enough, the synthesized CNPs possess an increased porosity of 326 m^2/g with uniform pore sizes of around 3.8 nm (Figure 2d and Table S1) due to the removal of PluronicF127 surfactant, which could be confirmed by the result of thermogravimetric (TGA) measurement (Figure S4). On the contrary, as for the CMPs, their specific surface area is significantly reduced from 405 m^2/g to 92 m^2/g, while the pore distribution becomes much broader compared with their microparticle precursors (Figure S3b, Figure S3c and Table S1). These phenomena highlight the importance of the materials in nanometer size on prevention of destruction of the morphology, size, and porous structure during pyrolysis, which is crucial for improving the ORR performance.[41] We also notice that the arrangement of the pores inside the CNPs is disordered (Figure 2c).

The composition of the formed CNPs is also analyzed by different characterization techniques including X-ray photoelectron spectroscopy (XPS), energy dispersive spectroscopy (EDS), X-ray diffraction (XRD) survey and Raman spectroscopy. XPS (Supporting Information, Figure S5a) and EDS (Figure S6) measurements indicate that the resultant CNPs are composed of C, N, O, and Fe, with average contents of ∼85.7 wt %, ∼4.4 wt %, ∼6.6 wt % and ∼3.3 wt %, respectively. Compared with MIL-88B-NH_3 NP precursors (Figure S5b),

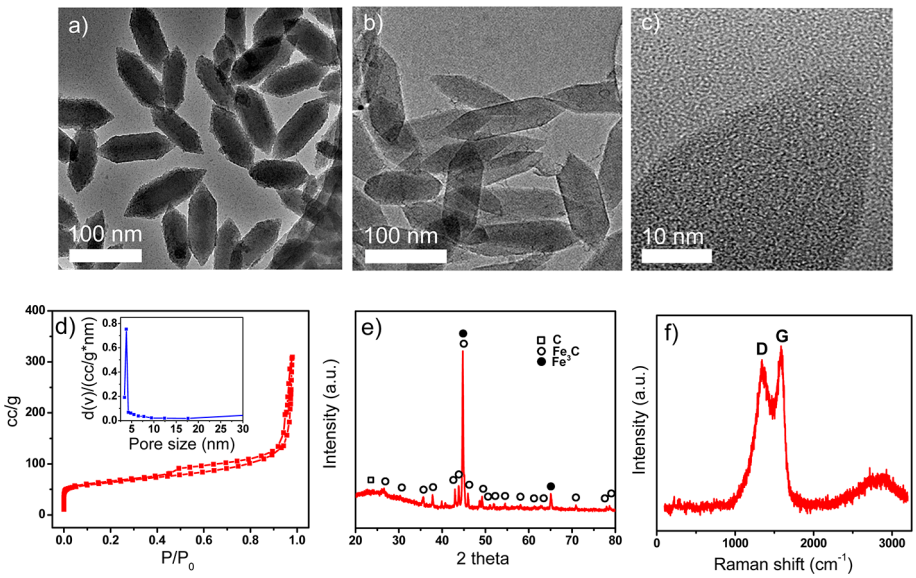

Figure 2. (a and b) TEM images of nanoscale MIL-88B-NH_3 and CNPs; (c) HRTEM image of CNPs; (d) N_2 adsorption−desorption isotherm of CNPs, and inset is the corresponding pore size distribution; (e) XRD pattern of CNPs; (f) Raman spectra of CNPs.

the C content in the CNPs is increased by ~37.3 wt %, whereas the content of N, O, and Fe is decreased by ~0.7 wt %, ~23.5 wt %, and ~13.0 wt %, respectively. Evidently, N, O, and Fe are partially lost after carbonization. The high-resolution C 1s XPS spectrum of CNPs presents several characteristic peaks, where the peak at 284.5 eV corresponds to the sp^2-hybridized graphitic carbon and the peaks at 285.9 and 288.3 eV are assigned to carbon in C−O and C−N bonds, respectively (Figure S7a). With respect to MIL-88B-NH_3 NP precursors (Figure S7b), the signal of sp^2 carbon of the CNPs is considerably increased accompanied by weakened signals of carbon in C−O and C−N bonds, suggesting partial loss of O- and N-based functional groups after pyrolysis (Figure S7). Such XPS observation is consistent with the element analysis results. Deconvolution of N 1s XPS peaks discloses that the amino-type nitrogen of the MIL-88B-NH_3 NPs (Figure S8b) is completely changed into pyridine-type nitrogen and quaternary-type nitrogen after conversion into the CNPs (Figure S8a), which should be caused by cyclization reactions as evidenced by the increased intensity of sp^2 carbon in C 1s XPS spectrum (Figure S7).[50−53] Such cyclization reactions not only give rise to the enhancement of the conductivity of CNPs, but also the formed nitrogen atoms in five- or six-membered rings could obviously improve the ORR catalytic activity compared with amino-type nitrogen.[50,51] The crystal structure of CNPs is further explored by XRD survey (Figure 2e), and amorphous carbon, crystalline Fe and Fe_3C are recognized according to the diffraction patterns of α-Fe (JCPDS No. 87-0722) and Fe_3C (JCPDS No. 89-2867). The amorphous carbon matrix, as well as the embedded Fe_3C, graphithe carbon, and Fe particles, is also discerned by the high-resolution TEM (HRTEM) images (Figure S9). One can note that carbon species nearby the Fe particles are catalyzed into layered graphite (Figure S9c). Nevertheless, the content of such layered graphite is relative low, and thus it cannot be distinguished by the XRD pattern (Figure 2e). The domination of the amorphous carbon in the CNPs can be confirmed by comparing intensity of the D-band peak at 1360 cm^{-1} and that of the G-band peak at 1590 cm^{-1} in the Raman spectroscopy (Figure 2f). The high ratio of I_D/I_G and the board peaks indicate that carbon inside the CNPs is highly disordered and significant edge plane sites are present.[47] Moreover, no Raman peak in the range of 200 to 600 cm^{-1} belonging to iron oxide can be found, implying that Fe or Fe_3C rather than iron oxide is formed in the carbonized products. Altogether, the above characterization results reveal that the original porous structures of the precursors are well preserved, the active species including Fe- and N-based compounds are generated, and the conductivity is enhanced for the pyrolytic products. All these features imply that the synthesized CNPs should possess superior ORR catalytic activity.

The ORR electrocatalytic activity of CNPs is first evaluated by cyclic voltammetry (CV) in O_2- or N_2-saturated 0.1 M KOH aqueous solution at room temperature. As shown in Figure 3a, a well-defined O_2 reduction peak centered at ca. 0.86 V (vs RHE) emerges when the electrolyte solution is saturated with O_2. As a comparison, under the identical experimental condition, the O_2 reduction peaks are located at 0.85 and 0.58 V for commercial Pt/C catalysts (20 wt % Pt, purchased from Johnson Matthey Corp.) and initial MIL-88B-NH_3 NPs, respectively, highlighting the superior catalytic activity of the CNPs (Supporting Information, Figure S10). Such an extraordinary electrocatalytic activity of CNPs, which even surpasses that of the commercial Pt/C, could be also confirmed by linear-sweep voltammetry (LSV) measurements on rotational disk electrode (RDE) (Figure 3b). It is clear that the ORR

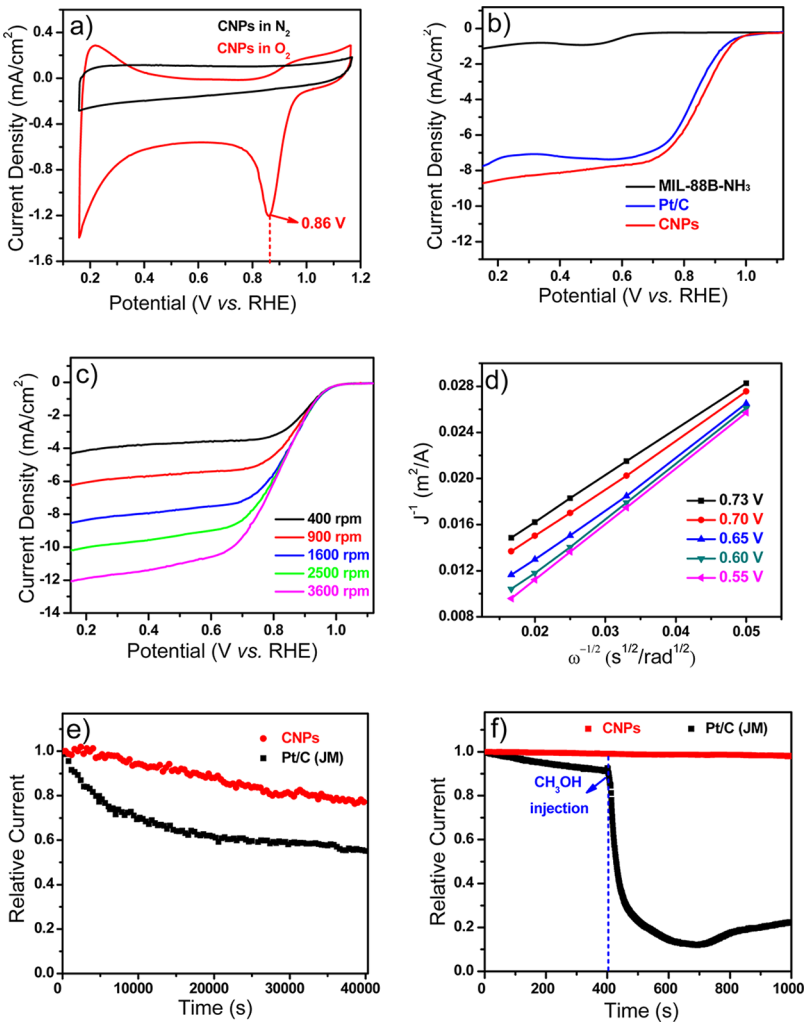

Figure 3. (a) CV curves of CNPs in N_2-saturated and O_2-saturated solution with 0.1 M KOH at a scan rate of 5 mV/s; (b) LSV curves of MIL-88B-NH_3 NPs, CNPs, and Pt/C at a rotation rate of 1600 rpm; (c) LSV curves of CNPs in O_2-saturated 0.1 M KOH with various rotation rates at a scan rate of 5 mV/s; (d) Koutecky–Levich plots of CNPs derived from LSV curves at different electrode potentials; (e) Chronoamperometric responses at 0.84 V in O_2-saturated 0.1 M KOH at CNP or Pt/C electrodes (1600 rpm) for 40000 s; (f) Chronoamperometric responses at 0.84 V in O_2-saturated 0.1 M KOH at CNP or Pt/C electrodes (1600 rpm) before and after addition of 2 M methanol. Note that the catalyst loading used in all electrochemical measurements is 0.39 mg/cm^2 for both CNPs and commercial Pt/C, which follows the reported literature.[50]

onset potential at CNPs (1.03 V) (defined as a potential required for reaching an ORR current density of 0.1 mA/cm^2) is more positive than that of Pt/C (1.01 V). Furthermore, the diffusion-limited current density of CNPs, 8.31 mA/cm^2 at 0.30 V, is considerably larger than that of commercial Pt/C, 7.08 mA/cm^2 at 0.30 V, highlighting that the porous CNPs with rich active sites are beneficial for both mass transport and catalytic conversion during an ORR process.[54] It is also worth mentioning that to our knowledge, the ORR activity of CNPs in this work outperforms all the reported non-noble metal catalysts (Supporting Information, Table S2). To gain deep insight into ORR mechanism involving the CNPs catalysts, LSV curves on RDE are recorded at different rotation rates (ω) from 400 to 3600 rpm (Figure 3c). Figure 3d presents the corresponding Koutecky–Levich (*K*–*L*) plots (J^{-1} *vs* $\omega^{1/2}$) against potentials and the linear plots suggest the first order reaction kinetics toward oxygen.[55] According to the *K*–*L* equation, the transferred electron number (*n*) per oxygen molecule for CNPs is calculated to be approximately 3.97 over the potential range from 0.55 to 0.73 V. The rotating ring-disk electrode (RRDE) measurement (Figure S11) further proves that there is negligible ring current, and the *n* calculated from the RRDE curves is about 3.98 over the potential range from 0.16 to 0.76 V. These experimental results demonstrate that a four-electron process is the dominating pathway for the oxygen reduction at the CNPs electrode, which benefits the construction of fuel cells with high efficiency.

Besides the activity, the stability is another key parameter for high-performance ORR catalysts. The ORR durability of both CNPs and commercial Pt/C is examined *via* the chronoamperometric method at 0.84 V (*vs* RHE) in an O_2-saturated 0.1 M KOH solution.

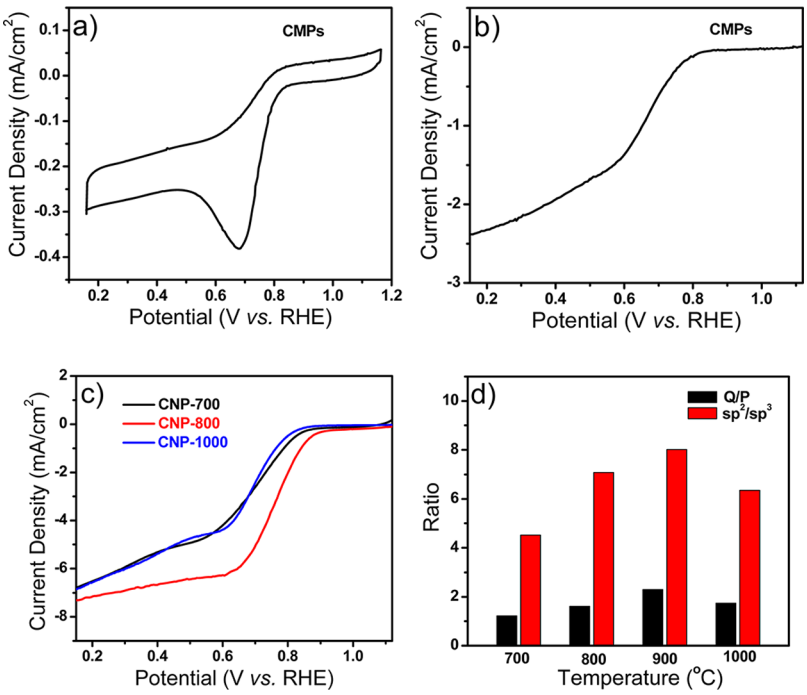

Figure 4. (a) CV curve of CMPs in O_2-saturated solution with 0.1 M KOH at a scan rate of 5 mV/s; (b) LSV curve of CMPs at a rotation rate of 1600 rpm; (c) LSV curves of CNPs-700, CNPs-800, and CNPs-1000 at a rotation rate of 1600 rpm; (d) Comparison of C and N species in samples pyrolyzed at different temperatures. Red bars represent the ratio between sp^2 carbon and sp^3 carbon, while black bars stand for the ratio between quaternary-type nitrogen and pyridine-type nitrogen. Note that the catalyst loading is 0.39 mg/cm^2 for all the samples, which follows the reported literature.[50]

Impressively, the current density of the CNPs electrode shows a much slower decay than that of the Pt/C electrode (Figure 3e). About 21% loss of the current density is occurred at the CNPs electrode after 40000 s, whereas the corresponding current loss at the Pt/C electrode under the same condition is as high as 47%. This result exemplifies that the CNPs catalyst is more stable than the commercial Pt/C catalyst. Since the ORR catalysts must be robust in real application systems, it is essential to test the tolerance of ORR catalysts toward methanol fuel. As shown in Figure 3f, a dramatic change is observed for the Pt/C catalyst in O_2-saturated 0.1 M KOH solution with injecting 2 M methanol, whereas no noticeable response for CNPs catalyst is detected under the same testing conditions. The big difference response to methanol is also found by investigating the CV behaviors of CNPs and Pt/C in the O_2-saturated 0.1 M KOH solution containing 2 M methanol (Supporting Information, Figure S12). As shown in Figure S12, there is no considerable change in the CV curve for CNPs after adding 2 M methanol (Figure S12a); however, the cathodic peak corresponding to the O_2 reduction disappears at the commercial Pt/C electrode coupled with one pair of peaks characteristic of methanol reduction/oxidation after adding 2 M methanol (Figure S12b). These results unambiguously disclose that the CNPs catalyst has higher selectivity and better methanol tolerance toward ORR than the commercial Pt/C catalyst.[7]

The important synthesis factors that influence the ORR have been investigated in details. CV measurement on the CMPs in O_2 saturated 0.1 M KOH aqueous solution shows a much negative O_2 reduction potential of 0.68 V (Figure 4a), while the corresponding LSV curve displays a very low current density of 2.32 mA/cm^2 at 0.30 V (Figure 4b). Compared with the CNPs (Supporting Information, Figure S1b), damage of the morphology and channel structure of the CMPs (Figure S2b) results in retarding O_2 diffusion and decreasing the active sites for ORR. Besides the size of the precursors, carbonization temperature is also crucial for improvement of ORR activity. Figure 4c presents the LSV curves on RDE at 1600 rpm in 0.1 M KOH solution when the products pyrolyzed at different temperatures are used as the ORR catalysts (the samples pyrolyzed at 700, 800, and 1000 °C are defined as CNPs-700, CNPs-800, and CNPs-1000, respectively). Evidently, all samples listed in Figure 4c show more negative onset potentials and lower limiting current densities when compared to the products pyrolyzed at 900 °C (red curve in Figure 3b), suggesting that 900 °C is the optimal pyrolysis temperature for obtaining highly active ORR catalysts. The best ORR performance of the CNPs pyrolyzed at 900 °C is also proved by comparing the transferred electron number (*n*) of the samples pyrolyzed at different temperatures (Figure S13). To investigate the origin of different electrochemical behaviors, XPS survey has been carried out (Figure 4d and Table S3). Analysis results reveal that the sample

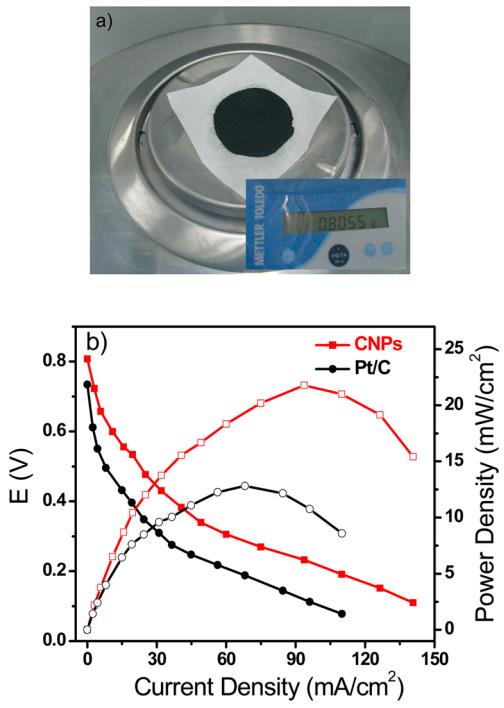

Figure 5. (a) Photo of CNPs at gram level obtained by one batch synthesis; (b) ADMFC single-cell performance constructed with CNPs and Pt/C catalysts at 60 °C under the same condition. According to the reported literature,[50,54] the loading amount of both CNPs and Pt/C is set to 3 mg/cm^2.

pyrolyzed at 900 °C possesses the maximum sp^2 carbon and quaternary-type nitrogen (Figure 4d) among all the samples, thus exhibiting the highest catalytic activity toward ORR. This observation is consistent with the reported theory that sp^2 carbon has better conductivity with respect to sp^3 carbon, while quaternary-type nitrogen possesses higher ORR activity compared with pyridine-type nitrogen.[54,56,57]

It should be stressed that such pyrolysis of the nanoscale MOFs is easily scaled up and the CNPs at gram level (0.8 g) could be achieved by one batch synthesis (Figure 5a), which would greatly facilitate their practical application. Alkaline direct methanol fuel cells (ADMFCs) based on either CNPs or Pt/C are constructed for comparative performance evaluation. Figure 5b highlights the working performance of different ADMFCs at 60 °C. Under the identical conditions, the open circuit voltage for the ADMFC equipped with the CNPs cathode (3 mg/cm^2 catalyst) is up to 0.81 V, which is higher than 0.74 V for the cell equipped with the Pt/C cathode (3 mg/cm^2 catalyst), indicating better methanol tolerance of the CNPs for ORR.[54,58,59] Furthermore, the peak power density and current density reach 22.7 mW/cm^2 and 93.9 mA/cm^2 at the cathode with the CNP catalyst, respectively, which are about 1.7 times and 1.4 times higher than that of the Pt/C cathode (13.5 mW/cm^2 and 68.1 mA/cm^2) suggesting that CNPs are a promising candidate for replacing conventional Pt in fuel cells. It should be stressed that to the best of our knowledge, 22.7 mW/cm^2 obtained from the CNP catalyst is the highest power density among the reported ADMFCs using non-noble catalysts (Supporting Information, Table S4). Such an outstanding performance of the ADMFC could be attributed to the excellent catalytic activity of the CNPs in oxygen reduction reaction.

CONCLUSION

In summary, a novel non-noble metal catalyst has been developed *via* pyrolysis of nanoscale MOFs with well-defined composition, structure, shape, and size. As-prepared CNPs are demonstrated to possess the superior electrocatalytic activity, stability, and tolerance toward ORR in the alkaline system, significantly beyond all the non-noble metal catalysts reported so far as well as the commercial Pt/C catalysts. The CNP catalysts at gram level are easily obtained and have been successfully applied in real ADMFC, which exhibits a record high output power density among the non-noble metal catalysts, evenly 1.7 times higher than that with commercial Pt/C catalysts. Detailed investigation discloses that the MOF nature and nanoscale tailoring determine the high performance of the carbonized products when used as the catalysts in ADMFC. This feasible strategy presents new opportunities for rational design of the codoped carbon nanomaterials with desirable composition, structure and morphology, which will have many applications in catalysis, energy, and environment.

EXPERIMENTAL SECTION

Materials. 2-Aminoterephthalic acid (H_2N-BDC, 99%), iron(III) chloride hexahydrate (98%), Nafion solution (5 wt %), and potassium hydroxide (99.9%) were purchased from Alfa Aesar. PluronicF127 was bought from Sigma-Aldrich. Carbon supported Pt (Pt/C, 20 wt % Pt) was bought from Johnson Matthey Corp. Acetic acid and methanol were obtained from Beijing Chemical Reagent Factory. All chemicals were used directly without further purification. Ultrapure water (18 MΩ) was supplied by a Millipore System (Millipore Q, USA).

Synthesis of Carbonized Nanocale Metal Organic Framework (CNPs). The MIL-88B-NH_3 NPs were synthesized according to the previously reported hydrothermal method with slight modification.[49] Briefly, 0.32 g of F127 was dissolved in 26.7 mL of deionized water, and 3.3 mL of 0.4 M $FeCl_3 \cdot 6H_2O$ aqueous solution (1.32 mmol) was added to the surfactant solution. The resulting solution was stirred for 1.5 h before 0.6 mL of acetic acid was injected. After the mixture was stirred for an additional 1.5 h, 120 mg (0.66 mmol) of H_2N-BDC was added. The reaction mixture was stirred for 2 h. Afterward, the reaction mixture was transferred into an autoclave and crystallized for 24 h at 110 °C. The dark brown solid product was recovered and washed several times with ethanol by centrifugation (at least five times) to remove the surfactant and excessive reactants. A large quantity of products could be obtained by increasing the amount of reactants. The microsized MIL-88B-NH_3 was prepared under the same synthetic conditions, except that both F127 and acetic acid were not added.

A porcelain cup with as-obtained MIL-88B-NH_3 NPs was put in the tube furnace under dynamic vacuum condition at 200 °C for 24 h. Then, the temperature was elevated to 900 °C at a speed of 1.5 °C/min and maintained for 6 h in argon gas. At last, the temperature was decreased to 30 °C at a speed of 2 °C/min. The CNPs-700, CNPs-800, and CNPs-1000 products were obtained at 700, 800, and 1000 °C, respectively.

Instrumentations. TEM imaging was performed on a FEI Tecnai G2 F20 electron microscope operated at 200 kV with the software package for automated electron tomography. SEM images were observed using Hitachi S4800 field emission scanning electron microscopy at 10 kV. XPS was recorded by a Thermo Scientific ESCALAB 250 Xi XPS system, in which the analysis chamber was 1.5×10^{-9} mbar and the size of the X-ray spot was 500 μm. XRD patterns were obtained by using a Panaltical X'Pert-pro MPD X-ray power diffractometer, with a Cu Kα irradiation source (λ =1.54056 Å), and a self-calibration process was performed with a SiO_2 internal standard sample prior to target measurement. Thermogravimetric analysis (TGA) was carried out by diamond TG/DTA from room temperature to 900 °C with a heating rate of 5 °C min^{-1} under an air flow.

Electrochemical Measurements. All the electrochemical data were measured in electrochemical station of Pine Instruments (model AFMSRCE). A conventional three-electrode system was used for electrochemical measurements. A mixture of 0.30 mL of deionized water, 0.30 mL of alcohol, 5 mg of CNPs or Pt/C catalysts, and 0.05 mL of Nafion solution (5 wt %) was subjected to ultrasonication for 12 h to obtain a homogeneous suspension. Next, 10 μL of the dispersion was uniformly dropped onto the freshly polished glassy carbon electrode (diameter = 0.5 cm), which was used as the working electrode. A Pt wire (φ = 0.5 mm) was utilized as a counter electrode, while an Ag/AgCl electrode saturated with KCl was used as the reference electrode. All the potentials reported in this work were expressed *versus* the reversible hydrogen electrode (RHE) based on the standard calculation method:[33] in 0.1 M KOH solution (pH = 13), E(RHE) = E(Ag/AgCl) + 0.964. Before each experiment, pure N_2 gas was bubbled through the solution for at least 25 min to remove the dissolved oxygen in the solution. The electrode was subjected to electrochemical treatment by potential cycling between 0.0 and 1.2 V at 50 mV/s in 0.1 M KOH until stable voltammogram curves were obtained. The cyclic voltammetry (CV) curves were obtained by cycling scan at room temperature after purging N_2 or O_2 for 15 min.

RDE measurement was carried out in the oxygen-saturated 0.1 M KOH solution at rotating rates varying from 400 to 3600 rpm, and with the scan rate of 5 mV/s. Linear-sweep voltammetry (LSV) on RDE was performed at the RDE of 5 mm in diameter. Koutecky–Levich plots (J^{-1} *vs* $\omega^{-1/2}$) in Figure 3d were analyzed at various electrode potentials. The slopes of their best linear fit lines were used to calculate the electron transfer number (n) on the basis of the Koutecky–Levich equation:[60,61]

$$1/J = 1/J_L + 1/J_K = 1/B\omega^{0.5} + 1/J_K \quad (1)$$

$$B = 0.64nFC_0D_0^{2/3}n^{-1/6}; \quad J_K = nFkC_d \quad (2)$$

where J was the measured current density, J_K and J_L were the kinetic- and diffusion-limiting current densities, ω was the angular velocity, n was the transferred electron number, F was the Faraday constant, C_0 was the bulk concentration of O_2, ν was the kinematic viscosity of the electrolyte, and k was the electron-transfer rate constant.

Another efficient method to estimate the electron transfer number (n) was the RRDE technique, in which the peroxide species produced at the disk electrode were detected by the ring electrode, and n was calculated from the ratio of the ring current (I_r) and the disk current (I_d) following the equation given below:[61]

$$n = 4\frac{I_d}{I_d + I_r/N} \quad (3)$$

where N was the collection efficiency (0.37) of the ring electrode.

Construction and Evaluation of Alkaline Direct Methanol Fuel Cell (ADMFC). Cell performance tests were carried out with ADMFCs using an electric load system (BT2000, Arbin Instrument, Inc.). The electrodes were fabricated by a spraying method. The ADMFC was composed of a membrane electrode assembly (MEA) with an area of 2.3 cm × 2.3 cm, which was sandwiched between two bipolar plates and fixed by two fixture plates. The loading amount of PtRu/C (40 wt % PtRu, Johnson Matthey Corp.) was set to be 3 mg/cm^2 at the anode, while either the loading amount of CNPs at the cathode was kept to be 3 mg/cm^2 or the loading amount of Pt/C (20 wt % Pt) at the cathode was kept to be 3 mg/cm^2. The single cell was then constructed by sandwiching an anion-exchange membrane (A201 Tokuyama Corporation) between the anode and the cathode by hot pressing at 130 °C for 60 s. The ADMFC was tested by an Arbin FCTs instrument at 60 °C. Briefly, 2 M methanol was pumped to the anode at a flux speed of 4.0 mL/min, while dry pure oxygen at a flux speed of 200 standard cubic centimeters per minute (sccm) was fed to the cathode. The fuel cell working conditions including the cell temperature, pressure, and reactant flux at the anode and the cathode were kept constant during the measurement.

Conflict of Interest: The authors declare no competing financial interest.

Acknowledgment. This work was supported financially by National Research Fund for Fundamental Key Project (2014CB931801, Z.Y.T.), National Natural Science Foundation of China (91023007 and 20773033 (S.Q.L.), 21025310 (Z.Y.T.)), and the New Century Excellent Talents in University, Outstanding Young Funding of Heilongjiang Province.

Supporting Information Available: Additional SEM images, TEM images, XPS analyses, and electrochemical measurements. This material is available free of charge *via* the Internet at http://pubs.acs.org.

REFERENCES AND NOTES

1. Mehta, V.; Cooper, J. Review and Analysis of PEM Fuel Cell Design and Manufacturing. *J. Power Sources* **2003**, *114*, 32–53.
2. Winter, M.; Brodd, R. What Are Batteries, Fuel Cells, and Supercapacitors? *Chem. Rev.* **2004**, *104*, 4245–4269.
3. Armand, M.; Tarascon, J. M. Building Better Batteries. *Nature* **2008**, *451*, 652–657.
4. Debe, M. K. Electrocatalyst Approaches and Challenges for Automotive Fuel Cells. *Nature* **2012**, *486*, 43–51.
5. Lu, Z.; Wang, H.; Kong, D.; Yan, K.; Hsu, P. C.; Zheng, G.; Yao, H.; Liang, Z.; Sun, X.; Cui, Y. Electrochemical Tuning of Layered Lithium Transitionmetal Oxides for Improvement of Oxygen Evolution Reaction. *Nat. Commom.* **2014**, *5*, 5345–5351.
6. Wang, Z. L.; Xu, D.; Xu, J. J.; Zhang, X. B. Oxygen Electrocatalysts in Metal-Air Batteries: From Aqueous to Nonaqueous Electrolytes. *Chem. Soc. Rev.*, DOI: 10.1039/c3cs60248f.
7. Katsounaros, I.; Cherevko, S.; Zeradjanin, A. R.; Mayrhofer, K. Oxygen Electrochemistry as a Cornerstone for Sustainable Energy Conversion. *Angew. Chem., Int. Ed.* **2014**, *53*, 102–121.
8. Tang, H. J.; Yin, H. J.; Wang, J. Y.; Yang, N.; Wang, D.; Tang, Z. Y. Molecular Architecture of Cobalt Porphyrin Multilayers on Reduced Graphene Oxide Sheets for High-Performance Oxygen Reduction Reaction. *Angew. Chem., Int. Ed.* **2013**, *125*, 5695–5699.
9. Yin, H. J.; Tang, H. J.; Wang, D.; Gao, Y.; Tang, Z. Y. Facile Synthesis of Surfactant-Free Au Cluster/Graphene Hybrids for High-Performance Oxygen Reduction Reaction. *ACS Nano* **2012**, *6*, 8288–8297.
10. Zheng, Y.; Jiao, Y. Zhu, Y. H.; Li, L. H.; Han, Y.; Chen, Y.; Du, A. J.; Jaroniec, M.; Qiao, S. Z. Hydrogen Evolution by a Metal-Free Electrocatalyst. *Nat. Commun.* DOI: 10.1038/ncomms4783.
11. Wang, H. L.; Yang, Y.; Liang, Y. Y.; Zheng, G. Y.; Li, Y. G.; Cui, Y.; Dai, H. J. Rechargeable Li-O_2 Batteries with a Covalently

Coupled $MnCo_2O_4$—Graphene Hybrid as an Oxygen Cathode Catalyst. *Energy Environ. Sci.* **2012**, *5*, 7931–7935.
12. Zhao, S. L.; Yin, H. J.; Du, L.; Yin, G. P.; Tang, Z. Y.; Liu, S. Q. Three Dimensional N-Doped Graphene/PtRu Nanoparticle Hybrids as High Performance Anode for Direct Methanol Fuel Cells. *J. Mater. Chem. A* **2014**, *2*, 3719–3724.
13. Zhang, W.; Wu, Z. Y.; Jiang, H. L.; Yu, S. H. Nanowire-Directed Templating Synthesis of Metal—Organic Framework Nanofibers and Their Derived Porous Doped Carbon Nanofibers for Enhanced Electrocatalysis. *J. Am. Chem. Soc.* **2014**, *136*, 14385–14388.
14. Tian, N.; Zhou, Z. Y.; Sun, S. G.; Yong, D.; Wang, Z. L. Synthesis of Tetrahexahedral Platinum Nanocrystals with High-Index Facets and High Electro-Oxidation Activity. *Science* **2007**, *316*, 732–735.
15. Lim, B.; Jiang, M. J.; Camargo, P. H. C.; Cho, E. C.; Tao, J.; Lu, X. M.; Zhu, Y. M.; Xia, Y. N. Pd—Pt Bimetallic Nanodendrites with High Activity for Oxygen Reduction. *Science* **2009**, *324*, 1302–1305.
16. Guo, S. J.; Zhang, S.; Sun, S. H. Tuning Nanoparticle Catalysis for the Oxygen Reduction Reaction. *Angew. Chem., Int. Ed.* **2013**, *52*, 8526–8544.
17. Yang, H.; Yin, Y. D. Shaping Nanostructures for Applications in Energy Conversion and Storage. *ChemSusChem* **2013**, *6*, 1781–1783.
18. Dai, F.; Zai, J. T.; Yi, R.; Gordin, M. L.; Sohn, H. S.; Chen, S. R.; Wang, D. H. Bottom-up Synthesis of High Surface Area Mesoporous Crystalline Silicon and Evaluation of Its Hydrogen Evolution Performance. *Nat. Commun.* **2014**, *5*, 3605–3615.
19. Joo, J. B.; Dahl, M.; Li, N.; Zaera, F.; Yin, Y. D. Tailored Synthesis of Mesoporous TiO_2 Hollow Nanostructures for Catalytic Applications. *Energy Environ. Sci.* **2013**, *6*, 2082–2092.
20. Wu, Z. Y.; Liang, H. W.; Li, C.; Hu, B. C.; Xu, X. X.; Wang, Q.; Chen, J. F.; Yu, S. H. Dyeing Bacterial Cellulose Pellicles for Energetic Heteroatom Doped Carbon Nanofiber Aerogels. *Nano Res.* **2014**, 10.1007/s12274-014-0546-4.
21. Jasinski, R. A New Fuel Cell Cathode Catalyst. *Nature* **1964**, *201*, 1212–1213.
22. Chen, P.; Xiao, T. Y.; Qian, Y. H.; Li, S. S.; Yu, S. H. A Nitrogen-Doped Graphene/Carbon Nanotube Nanocomposite with Synergistically Enhanced Electrochemical Activity. *Adv. Mater.* **2013**, *25*, 3192–3196.
23. Wen, Z. H.; Ci, S. Q.; Zhang, F.; Feng, X. L.; Cui, S. M.; Mao, S.; Luo, S. L.; He, Z.; Chen, J. H. Nitrogen-Enriched Core-Shell Structured Fe/Fe_3C-C Nanorods as Advanced Electrocatalysts for Oxygen Reduction Reaction. *Adv. Mater.* **2012**, *24*, 1399–1404.
24. Bashyam, R.; Zelenay, P. A Class of Non-precious Metal Composite Catalysts for Fuel Cells. *Nature* **2006**, *443*, 63–66.
25. Lefevre, M.; Proietti, E.; Jaouen, F.; Dodelet, J. P. Iron-Based Catalysts with Improved Oxygen Reduction Activity in Polymer Electrolyte Fuel Cells. *Science* **2009**, *324*, 71–74.
26. Liang, Y. Y.; Li, Y. G.; Wang, H. L.; Zhou, J. G.; Wang, J.; Regier, T.; Dai, H. J. Co_3O_4 Nanocrystals on Graphene as a Synergistic Catalyst for Oxygen Reduction Reaction. *Nat. Mater.* **2011**, *10*, 780–786.
27. Gong, K. P.; Du, F.; Xia, Z. H.; Durstock, M.; Dai, L. M. Nitrogen-Doped Carbon Nanotube Arrays with High Electrocatalytic Activity for Oxygen Reduction. *Science* **2009**, *323*, 760–764.
28. Li, Q. Q.; Zhang, S.; Dai, L. M.; Li, L. S. Nitrogen-Doped Colloidal Graphene Quantum Dots and Their Size-Dependent Electrocatalytic Activity for the Oxygen Reduction Reaction. *J. Am. Chem. Soc.* **2012**, *134*, 18932–18935.
29. Lee, J. S.; Park, G. S.; Kim, S. T.; Liu, M. L.; Cho, J. A Highly Efficient Electrocatalyst for the Oxygen Reduction Reaction: N-Doped Ketjenblack Incorporated into Fe/Fe_3C-Functionalized Melamine Foam. *Angew. Chem., Int. Ed.* **2013**, *125*, 1060–1064.
30. Zhao, D.; Shui, J. L.; Grabstanowicz, L. R.; Chen, C.; Commet, S. M.; Xu, T.; Lu, J.; Liu, D. J. Highly Efficient Non-precious Metal Electrocatalysts Prepared From One-Pot Synthesized Zeolitic Imidazolate Frameworks. *Adv. Mater.* **2014**, *26*, 1093–1097.
31. Nam, G.; Park, J.; Kim, S. T.; Shin, D. B.; Park, N.; Kim, Y.; Lee, J. S.; Cho, J. Metal-Free Ketjenblack Incorporated Nitrogen-Doped Carbon Sheets Derived From Gelatin as Oxygen Reduction Catalysts. *Nano Lett.* **2014**, *14*, 1870–1876.
32. Hu, Y.; Jensen, J. O.; Zhang, W.; Cleemann, L. N.; Xing, W.; Bjerrum, N. J.; Li, Q. F. Hollow Spheres of Iron Carbide Nanoparticles Encased in Graphitic Layers as Oxygen Reduction Catalysts. *Angew. Chem., Int. Ed.* **2014**, *53*, 3675–3679.
33. Chung, H. T.; Won, J. H.; Zelenay, P. Active and Stable Carbon Nanotube/Nanoparticle Composite Electrocatalyst for Oxygen Reduction. *Nat. Commun.* **2013**, *4*, 1922–1927.
34. Wu, G.; More, K. L.; Johnston, C. M.; Zelenay, P. High-Performance Electrocatalysts for Oxygen Reduction Derived From Polyaniline, Iron, and Cobalt. *Science* **2011**, *332*, 443–447.
35. Chen, P.; Wang, L. K.; Wang, G.; Gao, M. R.; Ge, J.; Yuan, W. J.; Shen, Y. H.; Xie, A. J.; Yu, S. H. Nitrogen-Doped Nanoporous Carbon Nanosheets Derived from Plant Biomass: An Efficient Catalyst for Oxygen Reduction Reaction. *Energy Environ. Sci.* **2014**, 10.1039/C4EE02531H.
36. Furukawa, H.; Cordova, K. E.; O'Keeffe, M.; Yaghi, O. M. The Chemistry and Applications of Metal—Organic Frameworks. *Science* **2013**, *341*, 974–986.
37. Cao, X. H.; Zheng, B.; Rui, X. H.; Shi, W. H.; Yan, Q. Y.; Zhang, H. Metal Oxide-Coated Three-Dimensional Graphene Prepared by the Use of Metal—Organic Frameworks as Precursors. *Angew. Chem., Int. Ed.* **2014**, *53*, 1428–1433.
38. Li, S. L.; Xu, Q. Metal—Organic Frameworks as Platforms for Clean Energy. *Energy Environ. Sci.* **2013**, *6*, 1656–1683.
39. Zhang, P.; Sun, F.; Xiang, Z. H.; Shen, Z. G.; Yun, J.; Cao, D. P. ZIF-Derived *in Situ* Nitrogen-Doped Porous Carbons as Efficient Metal-Free Electrocatalysts for Oxygen Reduction Reaction. *Energy Environ. Sci.* **2014**, *7*, 442–450.
40. Wei, W.; Liang, H. W.; Parvez, K.; Zhuang, X. D.; Feng, X. L.; Müllen, K. Nitrogen-Doped Carbon Nanosheets with Size-Defined Mesopores as Highly Efficient Metal-Free Catalyst for the Oxygen Reduction Reaction. *Angew. Chem., Int. Ed.* **2014**, *126*, 1596–1600.
41. Jiao, Y.; Zheng, Y.; Jaroniec, M.; Qiao, S. Z. Origin of the Electrocatalytic Oxygen Reduction Activity of Graphene-Based Catalysts: A Roadmap to Achieve the Best Performance. *J. Am. Chem. Soc.* **2014**, *136*, 4394–4403.
42. Li, J. S.; Li, S. L.; Tang, Y. J.; Li, K.; Zhou, L.; Kong, N.; Lan, Y. Q.; Bao, J. C.; Dai, Z. H. Heteroatoms Ternary-Doped Porous Carbons Derived From MOFs as Metal-Free Electrocatalysts for Oxygen Reduction Reaction. *Sci.Rep.* **2014**, *4*, 5130–5138.
43. Aijaz, A.; Fujiwara, N.; Xu, Q. From Metal—Organic Framework to Nitrogen-Decorated Nanoporous Carbons: Superior CO_2 Uptake and Highly Efficient Catalytic Oxygen Reduction. *J. Am. Chem. Soc.* **2014**, *136*, 6790–6793.
44. Zhang, L. J.; Su, Z. X.; Jiang, F. L.; Yang, L. L.; Qian, J. J.; Zhou, Y. F.; Li, W. M.; Hong, M. C. Highly Graphitized Nitrogen-Doped Porous Carbon Nanopolyhedra Derived from ZIF-8 Nanocrystals as Efficient Electrocatalysts for Oxygen Reduction Reactions. *Nanoscale* **2014**, *6*, 6590–6602.
45. Pandiaraj, S.; Aiyappa, H. B.; Banerjee, R.; Kurungot, S. Post Modification of MOF Derived Carbon *via* $g\text{-}C_3N_4$ Entrapment for an Efficient Metal-Free Oxygen Reduction Reaction. *Chem. Commun.* **2014**, *50*, 3363–3366.
46. Tian, J.; Morozan, A.; Sougrati, M. T.; Lefèvre, M.; Chenitz, R.; Dodelet, J.-P.; Jones, D.; Jaouen, F. Optimized Synthesis of Fe/N/C Cathode Catalysts for PEM Fuel Cells: A Matter of Iron-Ligand Coordination Strength. *Angew. Chem., Int. Ed.* **2013**, *125*, 7005–7008.
47. Hou, Y.; Huang, T. Z.; Wen, Z. H.; Mao, S.; Cui, S. M.; Chen, J. H. Metal-Organic Framework-Derived Nitrogen-Doped Core-Shell-Structured Porous Fe/Fe_3C@C Nanoboxes Supported on Graphene Sheets for Efficient Oxygen Reduction Reactions. *Adv. Energy Mater.* **2014**, 10.1002/aenm.201400337.

48. Liang, J.; Zhou, R. F.; Chen, X. M.; Tang, Y. H.; Qiao, S. Z. Fe-N Decorated Hybrids of CNTs Grown on Hierarchically Porous Carbon for High-Performance Oxygen Reduction. *Adv. Mater.* **2014**, *26*, 6074–6079.
49. Pham, M. H.; Vuong, G. T.; Vu, A. T.; Do, T.-O. Novel Route to Size-Controlled Fe-MIL-88B-NH_2 Metal−Organic Framework Nanocrystals. *Langmuir* **2011**, *27*, 15261–15267.
50. Ai, K. L.; Liu, Y. L.; Ruan, C. P.; Lu, L. H.; Lu, G.; (Max), Q. sp^2 C-Dominant N-Doped Carbon Sub-micrometer Spheres with a Tunable Size: A Versatile Platform for Highly Efficient Oxygen-Reduction Catalysts. *Adv. Mater.* **2013**, *25*, 998–1003.
51. Lai, L. F.; Potts, J. R.; Zhan, D.; Wang, L.; Poh, C. K.; Tang, C. H.; Gong, H.; Shen, Z. X.; Lin, J. Y.; Ruoff, R. S. Exploration of the Active Center Structure of Nitrogen-Doped Graphene-Based Catalysts for Oxygen Reduction Reaction. *Energy Environ. Sci.* **2012**, *5*, 7936–7942.
52. Yang, S. B.; Feng, X. L.; Wang, X. C.; Müllen, K. Graphene-Based Carbon Nitride Nanosheets as Efficient Metal-Free Electrocatalysts for Oxygen Reduction Reactions. *Angew. Chem., Int. Ed.* **2011**, *50*, 5339–5343.
53. Geng, D. S.; Chen, Y.; Chen, Y. G.; Li, Y. L.; Li, R. Y.; Sun, X. L.; Ye, S. Y.; Knights, S. High Oxygen-Reduction Activity and Durability of Nitrogen-Doped Graphene. *Energy Environ. Sci.* **2011**, *4*, 760–764.
54. Liu, J.; Sun, X. J.; Song, P.; Zhang, Y. W.; Xing, W.; Xu, W. L. High-Performance Oxygen Reduction Electrocatalysts Based on Cheap Carbon Black, Nitrogen, and Trace Iron. *Adv. Mater.* **2013**, *25*, 6879–6883.
55. Zhu, H. Y.; Zhang, S.; Huang, Y. X.; Wu, L. H.; Sun, S. H. Monodisperse $M_xFe_{3-x}O_4$ (M = Fe, Cu, Co, Mn) Nanoparticles and Their Electrocatalysis for Oxygen Reduction Reaction. *Nano Lett.* **2013**, *13*, 2947–2951.
56. Cong, H. P.; Wang, P.; Gong, M.; Yu, S. H. Facile Synthesis of Mesoporous Nitrogen-Doped Graphene: An Efficient Methanol-Tolerant Cathodic Catalyst for Oxygen Reduction Reaction. *Nano Energy* **2014**, *3*, 55–63.
57. Xiang, Z. H.; Xue, Y. H.; Cao, D. P.; Huang, L.; Chen, J. F.; Dai, L. M. Highly Efficient Electrocatalysts for Oxygen Reduction Based on 2D Covalent Organic Polymers Complexed with Non-precious Metals. *Angew. Chem., Int. Ed.* **2014**, *53*, 2433–2437.
58. Liu, M. M.; Lu, Y. Z.; Chen, W. PdAg Nanorings Supported on Graphene Nanosheets: Highly Methanol-Tolerant Cathode Electrocatalyst for Alkaline Fuel Cells. *Adv. Funct. Mater.* **2013**, *23*, 1289–1296.
59. Sun, X. J.; Zhang, Y. W.; Song, P.; Pan, J.; Zhuang, L.; Xu, W. L.; Xing, W. Fluorine-Doped Carbon Blacks: Highly Efficient Metal-Free Electrocatalysts for Oxygen Reduction Reaction. *ACS Catal.* **2013**, *3*, 1726–1729.
60. Lawson, D. R.; Whiteley, L. D.; Martin, C. R.; Szentimay, M. N.; Song, J. I. Oxygen Reduction at Nafion Film-Coated Platinum Electrodes: Transport and Kinetics. *J. Electrochem. Soc.* **1988**, *135*, 2247–2253.
61. Paulus, U. A.; Schmidt, T. J.; Gasteiger, H. A.; Behm, R. J. Oxygen Reduction on a High-Surface Area Pt/Vulcan Carbon Catalyst: A Thin-Film Rotating Ring-Disk Electrode Study. *J. Electroanal. Chem.* **2001**, *495*, 134–145.